Chemical Bonding Character and Physicochemical Properties of Mesoporous Zinc Oxide-Layered Titanate Nanocomposites

5 AUTHORS, INCLUDING:

Tae Woo Kim
Korea University
262 PUBLICATIONS   **4,250** CITATIONS

Yiseul Park
Daegu Gyeongbuk Institute of Science and T…
25 PUBLICATIONS   **903** CITATIONS

Wonyong Choi
Pohang University of Science and Technology
261 PUBLICATIONS   **23,857** CITATIONS

Jin-Ho Choy
Ewha Womans University
478 PUBLICATIONS   **9,875** CITATIONS

Chemical Bonding Character and Physicochemical Properties of Mesoporous Zinc Oxide-Layered Titanate Nanocomposites

Tae Woo Kim and Seong-Ju Hwang*

Center of Intelligent Nano-Bio Materials (CINBM), Division of Nano Sciences and Department of Chemistry, Ewha Womans University, Seoul 120-750, Korea

Yiseul Park and Wonyong Choi

School of Environmental Science and Engineering, Pohang University of Science and Technology, Pohang, Kyungbuk 790-784, Korea

Jin-Ho Choy

Center of Intelligent Nano-Bio Materials (CINBM), Division of Nano Sciences and Department of Chemistry, Ewha Womans University, Seoul 120-750, Korea

We have investigated the chemical bonding character and physicochemical properties of mesoporous zinc oxide-layered titanate nanocomposites synthesized by an exfoliation–restacking route. According to our analyses using X-ray diffraction, high resolution transmission electron microscopy, and N_2 adsorption–desorption isotherm measurements, nanocrystalline zinc oxides are stabilized not only in the interlayer space of the host titanate but also in the mesopores of the nanocomposites formed by the house-of-card type stacking of the crystallites. X-ray absorption spectroscopic analyses at Ti K- and Zn K-edges clearly demonstrate that nanocrystalline zinc oxides crystallized with a Wurzite type structure, and the lepidocrocite structure of the host titanate remains unchanged after hybridization and postcalcination. Upon hybridization with zinc oxide nanoparticles, the photocatalytic activity of layered titanate is enhanced with respect to the oxidative photodegradation of phenol and dichloroacetate. But of greater importance is that the chemical stability of guest zinc oxide against acidic corrosion is greatly improved by hybridization with layered titanate. In this regard, the present hybridization technique enables the application of chemically unstable nanostructured zinc oxides even in corrosive environments.

Introduction

Over the last several decades, extensive research activities have concentrated on semiconducting metal oxides and their wide applications as photocatalysts, luminescent and lasing materials, and solar cells.[1–6] Among semiconducting materials, zinc oxide has attracted intense research interests because of its diverse functionalities originating from its semiconducting nature.[3–6] Recently, many attempts have been made to synthesize nanostructured zinc oxides, with a goal of optimizing their functionalities through the tailoring of their electronic structure. In this context, the coupling of ZnO with other semiconducting materials has also received special attention as an alternative tool for tuning the ZnO electronic structure and functionality.[7] In fact, enhanced electron transfer between semiconductive components makes ZnO-coated TiO_2 a promising electrode for solar cells.[8] Also, the mixed oxide of ZnO–TiO_2 exhibits excellent performance as a recyclable catalyst for desulfurization reactions.[9] Very recently, the nanocomposite consisting of H_2-Ti_5O_{11} nanowires and ZnO nanocrystals was successfully synthesized through a hydrothermal reaction.[10] Taking into account the fact that the catalytic activity of these semiconductors becomes enhanced through the expansion of the surface

area, we believe the fabrication of porous structures consisting of ZnO and TiO_2 would be very advantageous for catalytic applications. Layered titanate, which is similar to yet slightly different from TiO_2 in terms of band structure near Fermi energy, is very useful for synthesizing a porous hybrid system containing zinc oxide nanoparticles through the formation of an intercalation complex. Moreover, it is highly feasible that the chemical stability of nanocrystalline zinc oxide can be greatly enhanced by its incorporation into two-dimensional inorganic solids, since the host layer can protect guest species from chemical corrosion. However, it is quite difficult to intercalate zinc oxide nanoparticles into two-dimensional metal oxides. The difficulty in preparing zinc oxide-layered metal oxide intercalation compounds stems from the rapid hydrolysis of zinc ions as well as the poor swelling ability of the host metal oxide.

In the present work, we have synthesized intercalative zinc oxide-layered titanate nanocomposites by adopting an exfoliation–restacking method. The crystal structure and porosity of the nanocomposites have been examined by X-ray diffraction (XRD), high resolution transmission electron microscopy (HR-TEM), and N_2 adsorption–desorption isotherm measurement. Also, we have investigated the local atomic arrangement and electronic configuration of zinc and titanium ions in the nanocomposites using X-ray absorption spectroscopy (XAS),

* To whom correspondence should be addressed. Tel.: +82-2-3277-4370. Fax: +82-2-3277-3419. E-mail: hwangsju@ewha.ac.kr.

Zinc Oxide-Layered Titanate Nanocomposites

J. Phys. Chem. C, Vol. 111, No. 4, 2007 **1659**

TABLE 1: Lattice Parameters, Surface Areas (S_{BET}), and CHN Contents of $Cs_{0.67}Ti_{1.83}\square_{0.17}O_4$, $H_{0.67}Ti_{1.83}\square_{0.17}O_4 \cdot H_2O$, Zinc Oxide−Titanate Nanocomposites, and Their Calcined Derivatives

| sample	a (Å)	b (Å)	c (Å)	S_{BET} ($m^2\ g^{-1}$)	C^a (%)	H^a (%)	N^a (%)
$Cs_{0.67}Ti_{1.83}\square_{0.17}O_4$	3.823	17.215	2.955				
$H_{0.67}Ti_{1.83}\square_{0.17}O_4 \cdot H_2O$	3.752	18.175	2.955				
ZT-**R**		21.41		41	3.25	1.66	
ZT-**R**, 200 °C				71	3.47	1.23	
ZT-**H**		12.03		115	3.70	1.44	
ZT-**H**, 200 °C		11.24		119	2.54	0.97	
ZT-**H**, 300 °C		10.86		134	2.07	0.78	
ZT-**H**, 400 °C				131	0.82	0.48	

a Error limits of C, H, and N analyses are 0.3% for C, 0.01% for H, and 0.2% for N.

which is very effective in studying low-dimensional and/or poorly crystalline materials.[11] The variation of the chemical stability of zinc oxide before and after hybridization was investigated by monitoring the dissolution of zinc ion in an acidic aqueous solution. Also, the decomposition of organic pollutants, like phenol and dichloroacetate (DCA), under UV−vis irradiation was examined to check out the variation of photocatalytic activity upon hybridization with zinc oxide.

Experimental Section

Sample Preparation. Pristine cesium titanate $Cs_{0.67}Ti_{1.83}\square_{0.17}O_4$ was prepared by calcining a stoichiometric mixture of Cs_2CO_3 and TiO_2 at 800 °C, as reported previously.[12] A proton exchange reaction for the pristine compound was carried out by reaction of the cesium titanate powder with 1 M HCl aqueous solution at room temperature for 4 days. During the proton exchange reaction, the HCl solution was replaced with a fresh one everyday. The exfoliation of the layered titanate lattice was achieved by reacting the protonic titanate with tetrabutylammonium hydroxide (TBA·OH) for more than 10 days. For effective exfoliation, the amount of TBA·OH was adjusted to yield the equivalent of exchangeable protons in $H_{0.67}Ti_{1.83}\square_{0.17}O_4 \cdot H_2O$.[12] After the reaction, a small fraction of incompletely exfoliated particles was eliminated through centrifugation at 12 000 rpm for 10 min, and the obtained colloidal suspension was used for the hybridization reaction. The sol solution of zinc acetate was prepared by reacting the aqueous solution of zinc acetate with *n*-propanol at 120 °C for 2 h. The zinc oxide-layered titanate nanocomposite was synthesized by reassembling the exfoliated colloidal titanate in the presence of the sol solution of zinc acetate at 80 °C for 2 h in a 50-mL autoclave with a Teflon liner (hereafter this sample is denoted as ZT-**H**).[13] Alternatively, the nanocomposite was obtained by refluxing the mixture of the above two solutions at 80 °C for 3 days (hereafter this sample is denoted as ZT-**R**). Flocculation occurred immediately after mixing these solutions, a result of the different charges on each solution's colloidal particles, causing electrostatic interaction. The resultant products were separated by centrifuging, washed thoroughly with distilled water, and dried.

Sample Characterization. The crystal structures of the zinc oxide-titanate nanocomposites were studied by powder XRD measurement using Ni-filtered Cu Kα radiation with a graphite diffracted beam monochromator. The chemical compositions of these samples were determined by performing induced coupled plasma (ICP) spectrometry and elemental CHN analysis, indicating the incorporation of zinc species into the layered titanate lattice with a Zn/Ti ratio of 2.1 for ZT-**R** and 1.8 for ZT-**H**.[13] As summarized in Table 1, the absence of nitrogen in the as-prepared nanocomposites highlights the complete ex-
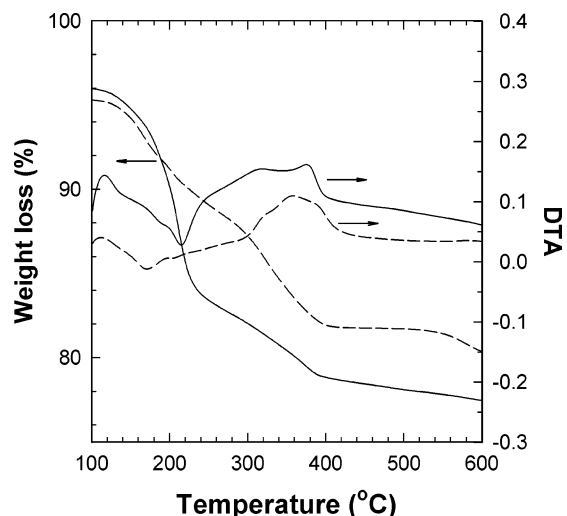
Figure 1. TG-DTA curves of ZT-**R** (solid lines) and ZT-**H** (dashed lines).

change of TBA for zinc species during the intercalation process. The thermal behaviors of the nanocomposites were examined by performing thermogravimetric−differential thermal analysis (TG-DTA) under an Ar atmosphere at the rate of 10 °C/min. As shown in Figure 1, both nanocomposites exhibit considerable weight loss below 400 °C.[13] An endothermic weight decrease in the temperature range of 100−250 °C is attributable to the dehydration and the dehydroxylation of guest species, whereas decomposition of the organic acetate groups is responsible for the exothermic weight loss in the higher temperature region. As listed in Table 1, although most of the acetate groups (about 80−90%) are decomposed during the synthesis, the as-prepared samples still contain small amount of acetates. Hence, heat treatment at 400 °C is necessary to eliminate residual carbon in the nanocomposite (Table 1). According to the weight loss of the first step, a larger amount of interlayer water molecules is in the ZT-**R** compound (2.3 H_2O per unit formula) than in the ZT-**H** (0.9 H_2O per unit formula). It is worthwhile to note here that a heat treatment at 200 °C of ZT-**R** leads to a slight increase in the relative weight percent of carbon because of the removal of a large amount of water molecules.[13]

The atomic arrangements of the nanocomposites were examined by performing HR-TEM measurement with a Philips-CM200 microscope at an accelerating voltage of 200 kV. To obtain cross-sectional images of the heterostructure, the sample was prepared by ultramicrotomy. The surface area and porosity of the nanocomposites were examined by volumetrically measuring nitrogen adsorption−desorption isotherms at liquid nitrogen temperature. The calcined samples were degassed at 150 °C for 2 h under vacuum before the adsorption measurement. XAS experiments were performed at Ti K- and Zn K-edges using an extended X-ray absorption fine structure (EXAFS) facility installed at the beam line 7C at the Pohang Accelerator Laboratory (PAL) in Pohang, Korea. The XAS measurements were carried out at room temperature in a transmission mode, using gas-ionization detectors. All of the present spectra were calibrated by measuring the spectrum of the Ti or Zn metal foil. The data analysis for the experimental spectra was performed by the standard procedure reported previously.[11] In the course of EXAFS fitting analysis for the reference ZnO, all of the coordination numbers (CNs) were fixed to the crystallographic values, but the amplitude reduction factor (S_0^2) was allowed to vary. On the basis of the S_0^2 estimated for the reference ZnO, the CNs of the nanocomposites were determined quantitatively to probe the effect of the nanocrys-
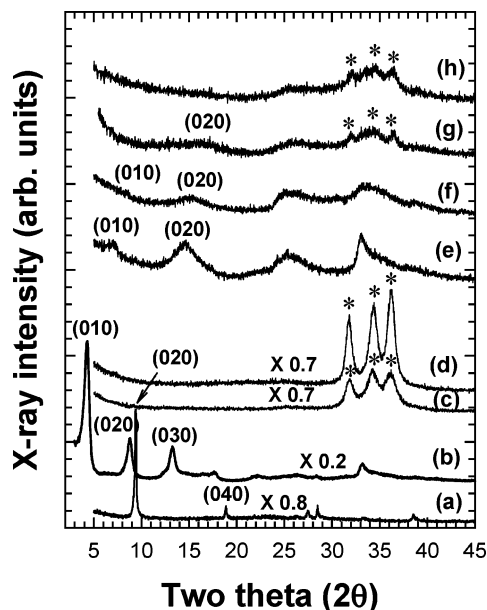
Figure 2. Powder XRD patterns for (a) the protonic titanate, (b) ZT-**R** and its derivatives calcined at (c) 200 and (d) 400 °C, and (e) ZT-**H** and its derivatives calcined at (f) 200, (g) 300, and (h) 400 °C. The asterisk symbols represent the Bragg reflections of ZnO.

talline nature on the local structure. On the other hand, all of the bond distances (R), Debye−Waller factors (σ^2), and energy shifts (ΔE) were set as variables, under the constraint that they were kept the same value for two adjacent (Zn−O) shells at ∼1.95−2.00 Å. Such constraints can be rationalized from the fact that the adjacent shells consisting of the same types of atoms at very close distances would possess nearly the same degree of energy shift and structural disorder.

Chemical Stability Test. The dissolution of zinc ions from the nanocomposites was tested in the acidic media with pH = 2, 4, and 6 in comparison with bare zinc oxide. After the reaction with the aqueous HCl solution for 5 h, the concentration of zinc ions in the supernant solution was analyzed with ICP analysis.

Photocatalytic Reactivity Test. Phenol and DCA were used as target substrates for the photocatalytic reactivity test. The substrate was added to an aqueous photocatalyst suspension in the glass reactor (40 mL) with a quartz window and then equilibrated for 1 h with stirring before illumination. The suspension was air-equilibrated. A 400-W Xe arc lamp (Oriel) was used as a light source. The light was passed through a 10-cm IR water filter and a cutoff filter ($\lambda > 300$ nm) and then focused onto the reactor. Sample aliquots were withdrawn intermittently with a 1-mL syringe during the illumination and filtered through a 0.45-μm poly(tetrafluoroethylene) (PTFE) filter (Millipore) to remove catalyst particles. Phenol was analyzed with a reverse-phase high performance liquid chromatograph (HPLC, Agilent 1100 series). The eluent consisted of a binary mixture of water containing 0.1% phosphoric acid and acetonitrile (80:20 by volume). The degradation of DCA and the concurrent production of chlorides were determined by using an ion chromatograph (IC, Dionex DX-120) equipped with a Dionex IonPac AS 14 (4 mm × 250 mm) column and a conductivity detector. The eluent solution was 3.5 mM Na$_2$-CO$_3$/1 mM NaHCO$_3$.

Results and Discussion

Powder XRD and HR-TEM Analyses. Figure 2 represents the powder XRD patterns of a protonic titanate and the zinc oxide-layered titanate nanocomposites prepared by reflux and

hydrothermal reactions, together with the patterns of the corresponding calcined derivatives. Both as-prepared nanocomposites show typical diffraction patterns of an intercalation complex with lattice expansion along the b-axis.[13] The least-square fitting analyses revealed that the nanocomposites of ZT-**R** and ZT-**H** show the expanded basal spacings of 20.4 and 12.0 Å corresponding to the gallery height of 12.9 and 4.5 Å. The larger basal spacing of ZT-**R** could be explained by its higher contents of water and zinc, as found from the TG analysis and chemical analysis. Taking into account the fact that ZT-**H** with smaller lattice expansion still has the higher concentration of Zn with respect to Ti (i.e., Zn/Ti = 1.8), we expect a fraction of the guest zinc species in this compound to exist in the pores of the nanocomposites as well as in the interlayer space of the host titanate. After the heat treatment at 200 °C, the ZT-**R** shows the complete disappearance of (0k0) reflections with the advent of distinct peaks of ZnO in the 30−40° region, clarifying the formation of zinc oxide. On the contrary, the ZT-**H** calcined at ≤300 °C retains a series of (0k0) reflections even with broader shape and depressed intensity, whereas these peaks vanish after the heat treatment at 400 °C. It is worthwhile to note here that, like the as-prepared samples, the (0k0) peaks still appear at a lower angle for the calcined derivatives than the pristine titanate. This finding underscores the maintenance of lattice expansion upon postcalcination, indicating the presence of the guest zinc oxide in the interlayer space of the calcined nanocomposites. In the high angle region, the ZT-**H** sample calcined at 300 °C shows very weak and diffusive ZnO peaks, reflecting the formation of zinc oxide nanoparticles. From the XRD result presented here, one can conclude that the nanocrystalline zinc oxides are formed not only in the interlayer of the host titanate with lattice expansion but also in the pores of the calcined nanocomposites.

The formation of the intercalative nanocomposites was further confirmed by a HR-TEM study, as presented in Figure 3. The cross-sectional views of the as-prepared nanocomposites display the assembly of parallel dark lines representing the titanate layers, clarifying the interstratification of layered titanate and zinc oxide nanoparticles. Furthermore, the basal spacing of the nanocomposites was estimated to be 2.1 nm for the as-prepared ZT-**R** and 1.2 nm for the as-prepared ZT-**H**, which is in good agreement with the b-axis lattice parameters determined from XRD analysis (Table 1). The maintenance of lattice expansion ($b = 10.8$ Å) of ZT-**H** after the postcalcination at 300 °C was also evidenced from the TEM study for this calcined sample.

N$_2$ Adsorption−Desorption Isotherm Analysis. We have carried out nitrogen adsorption−desorption isotherm measurements to probe the variation of surface area and pore structure upon hybridization and postcalcination. As plotted in Figure 4, both the as-prepared nanocomposites and their calcined derivatives show the BDDT type I and IV shape of isotherms, along with an H4-type hysteresis loop in the IUPAC classification.[13,14] This feature of the isotherm indicates the presence of the open slit-shaped capillaries with very wide bodies and narrow short necks. According to the fitting analysis based on the BET equation, the calcined derivatives of ZT-**H** show a highly expanded surface area of 119−134 m^2 g^{-1}, which is greater than the surface area of the ZT-**R** calcined at 200 °C (71 m^2 g^{-1}), as listed in Table 1. It should be noted that the mesoporous structure of the ZT-**H** is maintained even after calcination at 400 °C, underscoring the enhanced stability of the porous structure in this hydrothermally prepared compound. As can be seen clearly from Figure 4, all of the present nanocomposites show a distinct hysteresis in the region of $p/p_0 > 0.5$ with only
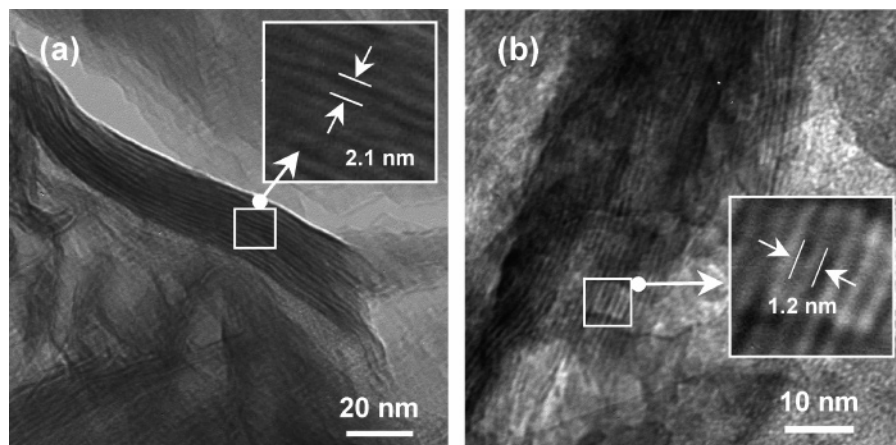
Zinc Oxide-Layered Titanate Nanocomposites

J. Phys. Chem. C, Vol. 111, No. 4, 2007 **1661**

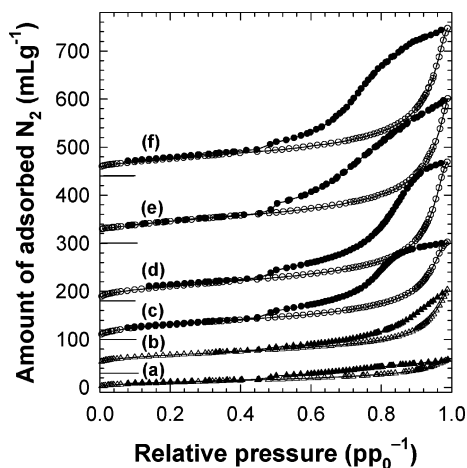**Figure 3.** HR-TEM images of (a) as-prepared ZT-**R** and (b) as-prepared ZT-**H**.

Figure 4. Nitrogen adsorption−desorption isotherms for (a) ZT-**R**, (b) its derivative calcined at 200 °C, and (c) ZT-**H** and its derivatives calcined at (d) 200, (e) 300, and (f) 400 °C.
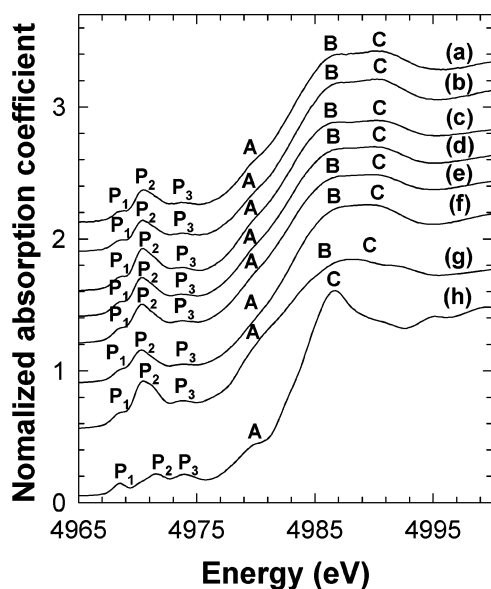

Figure 5. Ti K-edge XANES spectra of (a) ZT-**R**, (b) its derivative calcined at 200 °C, and (c) ZT-**H** and its derivatives calcined at (d) 200, (e) 300, and (f) 400 °C, together with the reference spectra of (g) cesium titanate and (h) TiO$_2$.

a negligible adsorption of N$_2$ molecules in a low relative pressure (p/p_0) region. This strongly suggests that most of the porosity in the present materials comes from mesopores in the stacked structure of the nanocomposite crystallites. The small contribu-

tion of the micropores to the total adsorption of nitrogen molecules is ascribed to the presence of residual carbon species and water molecules in the interlayer space and/or to the partial collapse of the pillared structure after the calcination.[13]

This conclusion is further supported by a pore distribution analysis using the Barrett−Joyner−Halenda (BJH) method, showing that the porosity of these materials originates mainly from mesopores with an average pore diameter of ∼3.5 nm. Judging from pore sizes and the basal increment upon hybridization, the observed mesopores should originate from the house-of-cards type stacking of composited nanosheets, not from the intercalation structure of the nanocomposites. Although the postcalcination gives rise to a reduction of the basal spacing of the intercalate compared with the pristine materials, the surface area and mesoporosity of the calcined derivatives are still much greater than those of the pristine titanate. This finding suggests that, even after the calcination, the mesoporous structure of the nanocomposites is maintained.

Ti K-Edge XANES Analysis. We have examined the chemical bonding nature of titanium ions in the nanocomposites, using X-ray absorption near-edge structure (XANES) analysis at the Ti K-edge. Figure 5 presents the Ti K-edge XANES spectra for the as-prepared zinc oxide-layered titanate nanocomposites and their calcined derivatives compared with those for the reference cases of TiO$_2$ and the pristine cesium titanate. All of the spectra presented here show three pre-edge peaks, P$_1$, P$_2$, and P$_3$, corresponding to the transitions from the core 1s level to the unoccupied 3d states.[15,16] In the main-edge region, there are three spectral features, A, B, and C, which originate from dipole-allowed 1s → 4p transitions.[16] In the case of the as-prepared nanocomposites, the overall spectral feature in the main-edge region is rather similar to that of the pristine cesium titanate, underscoring that the lepidocrocite structure of the titanate layer remains nearly the same upon hybridization with zinc oxide.

Furthermore, no marked spectral change appears after the calcination process. Of special note here is that the spectra of the ZT-**R** calcined at 200 °C and the ZT-**H** calcined at 400 °C are still similar to that of the as-prepared nanocomposites but fairly different from that of the TiO$_2$ reference. Although the XRD analysis of these compounds demonstrates the destruction of the pillared structure, the present XANES results clarify that the lepidocrocite structure of titanate sheets is still maintained after the collapse of the pillared structure. In this context, the disappearance of well-developed Bragg peaks after the calcinations at elevated temperature could be interpreted as a result of the elimination of long-range crystal order rather than the
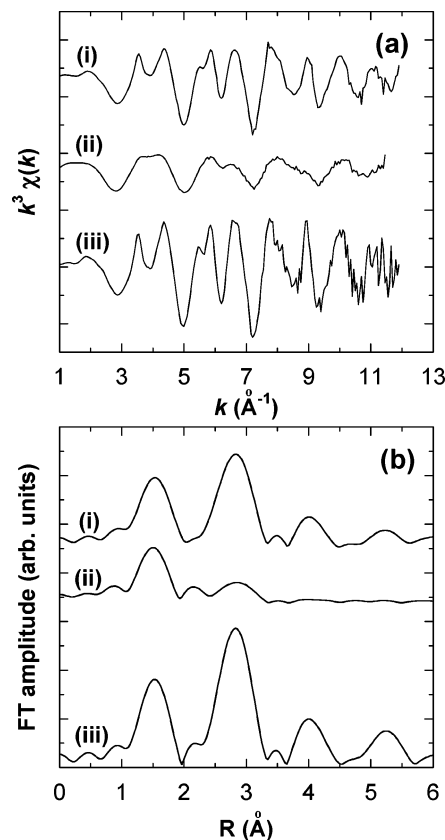
Figure 6. (a) k^3-weighted Zn K-edge EXAFS oscillations and (b) the Fourier transformed spectra for (i) ZT-**R** calcined at 200 °C, (ii) ZT-**H** calcined at 300 °C, and (iii) the reference ZnO.

Figure 7. Fourier filtered Zn K-edge EXAFS data for (a) ZT-**R** calcined at 200 °C, (b) ZT-**H** calcined at 300 °C, and (c) the reference ZnO. The open circles represent the experimental data and the solid lines represent the calculated data.

TABLE 2: Results of Non-Linear Least-Squares Curve Fittings for the Zn K-Edge EXAFS Spectra of the Calcined Nanocomposites and the Reference ZnO

sample	bond	CN	R (Å)	σ^2 ($10^{-3} \times$ Å^2)
ZT-**R**, 200 °C[a]	(Zn−O)	3.0	1.98	6.09
	(Zn−O)	1.0	1.99	6.09
ZT-**H**, 300 °C[b]	(Zn−O)	2.4	1.95	6.38
	(Zn−O)	0.8	1.97	6.38
reference ZnO[c]	(Zn−O)	3	1.97	5.08
	(Zn−O)	1	1.99	5.08

[a] Curve fitting analysis was performed for the range of 1.104−R−2.086 Å and 3.30−k−10.30 Å^{-1}. [b] Curve fitting analysis was performed for the range of 1.135−R−2.117 Å and 3.30−k−10.45 Å^{-1}. [c] Curve fitting analysis was performed for the range of 1.166−R−1.963 Å and 3.30−k−9.70 Å^{-1}.

structural transition of the layered titanate component into a rutile or anatase TiO$_2$ phase. Considering the fact that the protonic layered titanate turns into anatase TiO$_2$ just above 200 °C,[17] one can conclude that this finding provides strong evidence of the enhancement of the structural stability of the titanate layer through the hybridization process.

Zn K-edge XANES/EXAFS Analyses. We have also investigated the local crystal structure and the oxidation state of zinc ion using Zn K-edge XANES and EXAFS spectroscopy. According to XANES analysis, both of the as-prepared nanocomposites show poorly resolved peaks in the energy region of 9664−9668 eV, which is typical of nanocrystalline zinc oxide.[13,18] The calcination of the ZT-**R** at 200 °C leads to the bulk ZnO-like spectral features, but all of the calcined products of ZT-**H** retain poorly resolved XANES features. This confirms that most of the zinc species in the calcined ZT-**H** exist as a nanocrystalline zinc oxide. In fact, such poorly resolved spectral features were also observed for zinc oxide nanocrystals stabilized in the interlayer space of montmorillonite clays.[19]

We have determined quantitatively the structural parameters of the intercalated zinc oxide species by performing EXAFS analysis. The k^3-weighted Zn K-edge EXAFS spectra for the calcined nanocomposites and the reference ZnO are plotted in Figure 6a. The experimental EXAFS spectrum of the calcined ZT-**R** is nearly identical to that of the reference ZnO; however, the amplitude of the EXAFS oscillation is much weaker for the calcined ZT-**H** than for the other compounds. In spite of such amplitude differences, the overall features of EXAFS oscillation of both of the nanocomposites are rather similar to that of the reference ZnO, strongly suggesting a close relation of the local structures among these compounds.
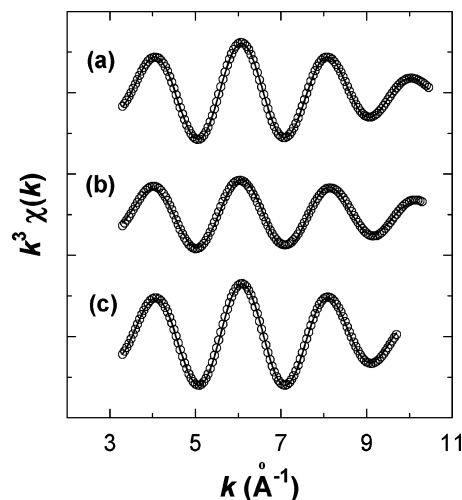
In the Fourier transform (FT) diagrams of Figure 6b, all of the present compounds display two intense peaks in the R range of 1.0−3.5 Å, which correspond to the (Zn−O) shells and (Zn−Zn) bonding pairs in corner-shared ZnO$_4$ tetrahedra. In contrast to the ZT-**R** calcined at 200 °C, the distant FT peaks at ~2.8 Å of the ZT-**H** calcined at 300 °C appear much weaker than those of ZnO. This is indicative of the limited crystal growth of ZnO in the confined space of the nanocomposite. The first FT peak emanating from Zn−O bonds was isolated by inverse Fourier transformation to k space. The resulting $k^3\chi(k)$ Fourier filtered EXAFS oscillations are shown in Figure 6, and the curve fittings were carried out on them to determine the structural parameters. As plotted in Figure 7, the Fourier filtered spectrum of the reference ZnO was quite reproducible with the Wurzite structure, and the obtained structural parameters presented in Table 2 are in good agreement with the crystallographic values, verifying the reliability of the present fitting analyses.

Like the reference zinc oxide, the Fourier filtered spectra of both of the nanocomposites were quite reproducible with the Wurzite structure. As listed in Table 2, the zinc ions are stabilized in the ZnO$_4$ tetrahedra with (Zn−O) bond distances of 1.98−1.99 Å for the ZT-**R** calcined at 200 °C and 1.95−1.97 Å for the ZT-**H** calcined at 300 °C. These bond distances are comparable with the (Zn^{II}−O) bond lengths in bulk ZnO (1.97−1.99 Å). As summarized in Table 2, the ZT-**H** calcined at 300 °C shows smaller CN values than ZnO and the ZT-**R** calcined at 200 °C, a result of the limited growth of zinc oxide nanoparticles in the calcined ZT-**H**.
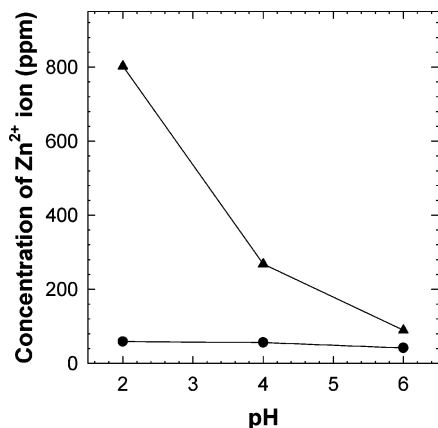
Zinc Oxide-Layered Titanate Nanocomposites

J. Phys. Chem. C, Vol. 111, No. 4, 2007 **1663**

Figure 8. pH-dependent variation of zinc concentration dissolved from ZT-**H** calcined at 300 °C (circles) and bare ZnO (triangles). The dissolution experiments were performed in acidic media with pH = 2, 4, and 6 for 5 h.

Chemical Stability Measurements. The chemical stability of the zinc oxide incorporated into the nanocomposites was evaluated by monitoring the time-dependent dissolution of zinc ions in acidic solutions with pH = 2, 4, and 6. As shown in Figure 8, the concentration of zinc ions dissolved from the bare zinc oxide becomes greater as the pH is lowered. Eventually, the zinc oxide is completely dissolved within 5 min for the case of the most acidic solution with pH = 2. On the contrary, for all pH regions presented here, the dissolution of zinc ions is much lower for the nanocomposite than for the bare zinc oxide. Moreover, there is no distinct pH dependence on zinc dissolution, indicating the enhanced chemical stability of zinc oxide through the hybridization. The present results clearly demonstrate that hybridization with the titanate improves the chemical stability of the guest zinc oxide nanocrystals. Considering that the poor stability of nanocrystalline zinc oxide in the face of chemical corrosion prohibits the use of ZnO in a solution with low pH, we conclude that the present protection strategy through hybridization can provide a very valuable method to widen the application fields of zinc oxide. On the basis of the experimental findings presented here, it is clear that the zinc oxide species are stabilized in the interlayer space of the nanocomposites and in the mesopores formed by the house-of-cards stacking of nanocomposite crystallites, as well. The observed suppression of zinc dissolution upon hybridization underscores that the zinc oxide particles in the interlayer space and in the mesopores are all protected by the host titanate layers. Furthermore, the negligible dissolution of zinc ions allows us to rule out the existence of zinc oxide on the sample surface directly exposed to the acidic media.

Photocatalytic Activity Tests. The photocatalytic activity of the zinc oxide-layered titanate nanocomposites was evaluated by measuring the time-dependent degradation of phenol in an illuminated catalyst suspension. As illustrated in Figure 9, the zinc oxide-layered titanate nanocomposites induce distinct photodegradation of phenol under UV−vis light irradiation, showing the photocatalytic activity of these materials. In comparison with the pristine cesium titanate, the nanocomposites exhibit higher activities, strongly suggesting the positive effect of hybridization. Such an improvement of photocatalytic activity would be a result of the hybridization of highly active ZnO nanoparticles as well as the enhancement of the lifetime of transient electrons and/or holes through a charge transfer between host and guest. Among the nanocomposites, the calcined samples at elevated temperature are more active than the as-prepared ones. This calcination effect could be linked to
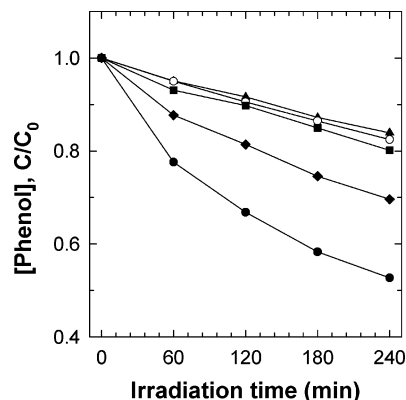

Figure 9. Time-dependent profiles of the phenol concentration upon photocatalytic degradation under UV−vis radiation ($\lambda > 300$ nm) with ZT-**R** calcined at 200 °C (closed circles), ZT-**H** calcined at 200 (closed triangles), 300 (closed squares), and 400 °C (closed diamonds), and the pristine $Cs_{0.67}Ti_{1.83}\square_{0.17}O_4$ (open circles).
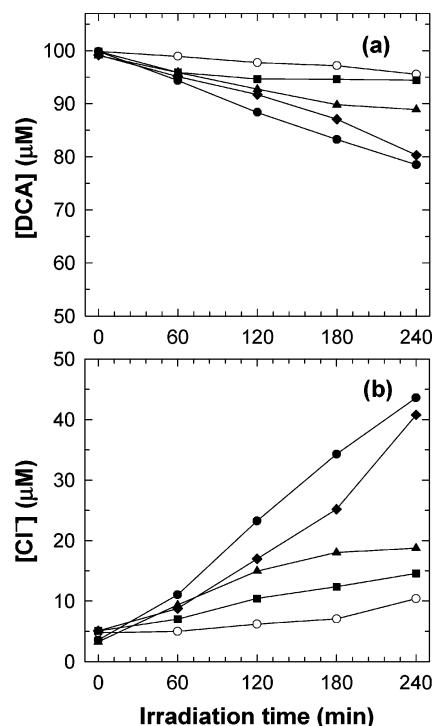

Figure 10. Time-dependent profiles of (a) DCA and (b) the evolved chloride ion upon the photocatalytic degradation under UV−vis radiation ($\lambda > 300$ nm) with ZT-**R** calcined at 200 °C (close circles), ZT-**H** calcined at 200 (close triangles), 300 (close squares), and 400 °C (close diamonds), and the pristine $Cs_{0.67}Ti_{1.83}\square_{0.17}O_4$ (open circles).

both of the following two factors. One is the removal of residual organic species in the nanocomposite, which makes the photocatalyst more active. The other factor is the improved electronic coupling and electrical connectivity between the titanate layer and the zinc oxide particle, which modifies the electronic structure to enhance the lifetime of transient electrons and/or holes through the spatial separation.

In addition, the degradation of DCA under UV−vis light irradiation was tested. Figure 10 clearly demonstrates that the nanocomposites also possess significant photocatalytic activity for the degradation of DCA. The production of chloride ions occurs concurrently with the degradation of DCA (see Figure 10b), which confirms that the removal of DCA is indeed a result of the light-induced degradation, not the adsorption. As can be seen clearly from Figure 10, the zinc oxide-layered titanate

1664 *J. Phys. Chem. C, Vol. 111, No. 4, 2007*

Kim et al.

nanocomposites induce a more effective photodegradation of DCA than the pristine cesium titanate, confirming the positive effect of hybridization. However, the photocatalytic activity of the nanocomposites is lower than that of the reference ZnO (not shown here). This seems to be related to the location of active ZnO sites within the host titanate layers, which hinders the mass transfer of substrates and the availability of photons to the active sites. Nevertheless*,* hybridization of the nanocomposites compensates for the lower photocatalytic activity (compared with bare ZnO) with a marked enhancement of the chemical stability of ZnO against chemical and photochemical corrosion. This advantage guarantees the validity of the nanocomposites as useful materials that are applicable to corrosive environments.

Conclusion

We have synthesized and characterized porous zinc oxide-layered titanate nanocomposites. In the nanocomposites, nanocrystalline zinc oxides with Wurzite type structure are stabilized not only in the interlayer space of the lepidocrocite-structured host titanate layers but also in the mesopores of the house-of-cards type stacking structure of the nanocomposite crystallites. Hybridization with zinc oxide was found to improve the photocatalytic activity of layered titanate with respect to the photodegradation of organic pollutants. Of special importance is that the corrosion of zinc oxide in an acidic solution is significantly suppressed by hybridization with layered titanate, underscoring the usefulness of hybridization with layered inorganic solids for the stabilization of nanostructured ZnO. Our current project is the hybridization of one-dimensional zinc oxide nanorods with layered metal oxide nanosheets to enhance the chemical stability of the nanostructured ZnO which will allow for the application of this material in acidic media.

References and Notes

(1) Honda, K.; Fujishima, A. *Nature* **1972**, *238*, 37.

(2) (a) Hoffmann, M. R.; Martin, S. T.; Choi, W.; Bahnemann, D. W. *Chem. Rev.* **1995**, *95*, 69. (b) Mills, A.; Hunte, S. L. *J. Photochem. Photobiol., A* **1997**, *108*, 1. (c) Yeong, I. K.; Samer, S.; Munir, J. H.; Mallouk, T. E. *J. Am. Chem. Soc.* **1991**, *113*, 9561.

(3) Spanhel, L.; Anderson, M. A. *J. Am. Chem. Soc.* **1991**, *113*, 2826.

(4) (a) Yang, J. L.; An, S. J.; Park, W. I.; Yi, G. C.; Choi, W. *Adv. Mater.* **2004**, *16*, 1661. (b) Rensmo, H.; Keis, K.; Lindstrom, H.; Solbrand, A.; Hagfeldt, A.; Lindquist, S. E.; Wang, L. N.; Muhammed, M. *J. Phys. Chem. B* **1997**, *101*, 2598.

(5) Huang, M. H.; Mao, S.; Feick, H.; Yan, H.; Wu, Y.; Kind, H.; Weber, E.; Russo, R.; Yang, P. *Science* **2001**, *292*, 1897.

(6) Zamfirescu, M.; Kavokin, A.; Gil, B.; Malpuech, G.; Kaliteevski, M. *Phys. Rev. B* **2002**, *65*, 161205.

(7) Marci, G.; Augugliaro, V.; Lopez-Munoz, M. J.; Martin, C.; Palmisano, L.; Rives, V.; Schiavello, M.; Tilley, R. J. D.; Venezia, A. M. *J. Phys. Chem. B* **2001**, *105*, 1033.

(8) Wang, Z. S.; Huang, C. H.; Huang, Y. Y.; Hou, Y. J.; Xie, P. H.; Zhang, B. W.; Cheng, H. M. *Chem. Mater.* **2001**, *13*, 678.

(9) (a) Hatori, M.; Sasaoka, E.; Uddin, M. A. *Ind. Eng. Chem. Res.* **2001**, *40*, 1884. (b) Lew, S.; Jothimurugesan, K.; Flytzani-Stephanopoulos, M. *Ind. Eng. Chem. Res.* **1989**, *28*, 535. (c) Woods, M. C.; Gangwal, S. K.; Jothimurugesan, K.; Harrison, D. P. *Ind. Eng. Chem. Res.* **1990**, *29*, 1160.

(10) Yang, H. G.; Zeng, H. C. *J. Am. Chem. Soc.* **2005**, *127*, 270.

(11) (a) Choy, J. H.; Hwang, S. J.; Park, N. G. *J. Am. Chem. Soc.* **1997**, *119*, 1624. (b) Hwang, S. J.; Kwon, C. W.; Portier, J.; Campet, G.; Park, H. S.; Choy, J. H.; Huong, P. V.; Yoshimura, M.; Kakihana, M. *J. Phys. Chem. B* **2002**, *106*, 4053.

(12) (a) Sasaki, T.; Watanabe, M.; Hashizume, H.; Yamada, H.; Nakazawa, H. *J. Am. Chem. Soc.* **1996**, *118*, 8329. (b) Sasaki, T.; Watanabe, M. *J. Am. Chem. Soc.* **1998**, *120*, 4682.

(13) Kim, T. W.; Hur, S. G.; Hwang, S. J.; Choy, J. H. *Chem. Commun.* **2006**, 220−222.

(14) (a) Sing, K. S. W.; Everett, D. H.; Haul, R. A. W.; Moscou, L.; Pierotti, R. A.; Rouquerol, J.; Siemieniewska, T. *Pure Appl. Chem.* **1985**, *57*, 603−619. (b) Carrado, K. A.; Csenesits, R.; Thiyagarajan, P.; Seifert, S.; Macha, S. M.; Harwood, J. S. *J. Mater. Chem.* **2002**, *12*, 3228.

(15) Hess, N. J.; Balmer, M. L.; Bunker, B. C.; Conradson, S. D. *J. Solid State Chem.* **1997**, *129*, 206.

(16) Hur, S. G.; Park, D. H.; Kim, T. W.; Hwang, S. J. *Appl. Phys. Lett.* **2004**, *85*, 4130.

(17) Yin, S.; Uchida, S.; Fujishiro, Y.; Aki, M.; Sato, T. *J. Mater. Chem.* **1999**, *9*, 1191.

(18) Park, N. G.; Kang, M. G.; Kim, K. M.; Ryu, K. S.; Chang, S. H.; Kim, D. K.; van de Langemaat, J.; Benkstein, K. D.; Frank, A. J. *Langmuir* **2004**, *20*, 4246.

(19) Hur, S. G.; Kim, T. W.; Hwang, S. J.; Hwang, S. H.; Yang, J. H.; Choy, J. H. *J. Phys. Chem. B* **2006**, *110*, 1599.